Computer Modeling in Engineering & Sciences

Tech Science Press

DOI: 10.32604/cmes.2023.031372

ARTICLE

Radiative Blood-Based Hybrid Copper-Graphene Nanoliquid Flows along a Source-Heated Leaning Cylinder

Siti Nur Ainsyah Ghani[1] and Noor Fadiya Mohd Noor[1,2,*]

[1]Institute of Mathematical Sciences, Faculty of Science, Universiti Malaya, Kuala Lumpur, 50603, Malaysia

[2]Center for Data Analytics Consultancy & Services (UM-CDACS), Faculty of Science, Universiti Malaya, Kuala Lumpur, 50603, Malaysia

*Corresponding Author: Noor Fadiya Mohd Noor. Email: drfadiya@um.edu.my

Received: 07 June 2023 Accepted: 13 September 2023 Published: 30 December 2023

ABSTRACT

Variant graphene, graphene oxides (GO), and graphene nanoplatelets (GNP) dispersed in blood-based copper (Cu) nanoliquids over a leaning permeable cylinder are the focus of this study. These forms of graphene are highly beneficial in the biological and medical fields for cancer therapy, anti-infection measures, and drug delivery. The non-Newtonian Sutterby (blood-based) hybrid nanoliquid flows are generalized within the context of the Tiwari-Das model to simulate the effects of radiation and heating sources. The governing partial differential equations are reformulated into a nonlinear set of ordinary differential equations using similar transformational expressions. These equations are then transformed into boundary value problems through a shooting technique, followed by the implementation of the bvp4c tool in MATLAB. The influences of various parameters on the model's non-dimensional velocity and temperature profiles, reduced skin friction, and reduced Nusselt number are presented for detailed discussions. The results indicated that Cu-GNP/blood and Cu-GO/blood hybrid nanofluids exhibit the lowest and highest velocity distributions, respectively, for increased nanoparticles volume fraction, curvature parameter, Sutterby fluid parameter, Hartmann number, and wall permeability parameter. Conversely, opposite trends are observed for the temperature distribution for all considered parameters, except the mixed convection parameter. Increases in the reduced skin friction magnitude and the reduced Nusselt number with higher values of graphene/GO/GNP nanoparticle volume fraction are also reported. Finally, GNP is identified as the superior heat conductor, with an average increase of approximately 5% and a peak of 7.8% in the reduced Nusselt number compared to graphene and GO nanoparticles in the Cu/blood nanofluids.

KEYWORDS

Hybrid nanofluid; sutterby fluid; tiwari-das model; thermal radiation; graphene; graphene oxides; graphene nanoplatelets

Nomenclature

B_0	External magnetic field (T)
c_p	Specific heat capacity (J/kgK)
H_{w*}	Uniform surface mass flux (kg/(m^{2}s))
l	Reference length (m)
m	Flow component index (–)

n	Nanoparticle shape factor (–)
Q^*	Source of heating (J)
q_w	Flux of heat (W/m^2)
Re	Reynolds number (–)
T	Temperature (K)
u, v	Velocity associated components (m/s)
U_0	Velocity of free stream (m/s)

Greek Symbols

$beta_T$	Coefficient for thermal expansion (1/K)
$sigma$	Electrical conductivity (S/m)
tau_w	Shear stress (Pa)
ϕ_1	Nanoparticles volume fraction for Cu (–)
ϕ_2	Nanoparticles volume fraction for graphene/GO/GNP (–)

Subscripts

f	Based fluid
nf	Mono/single nanofluids
hnf	Duo/hybrid nanofluids
$s1$	Cu solid nanoparticles
$s2$	Graphene/GO/GNP solid nanoparticles
w	Wall surface of a cylinder
0	Initial or reference
∞	Ambient

1 Introduction

The boundary layer is a fundamental concept in understanding fluid transportation over a surface from theoretical fluid mechanics perspectives, pioneered by Prandtl in 1904 [1]. Conventional liquids, such as oil, ethylene glycol (EG), and water, used in various mechanical and technical operations, typically exhibit poor thermal conductivity, limiting the heat transfer efficiency for specific engineering processes. In 1993, Choi et al. [2] introduced a nanotechnology-based fluid aimed at enhancing energy efficiency and heat transfer capacity. As a result, nanofluids became prominent in heat transfer applications, including the biomedical and pharmaceutical sectors, microelectronics, magma solidification, cooling and heating exchangers, drug delivery, and food manufacturing. A mono nanofluid is defined as a single type of solid nanoparticle homogeneously dispersed in an ordinary liquid. Recent attention has shifted toward the introduction of multiple different nanoparticles suspended in that ordinary liquid, referred to as hybrid, ternary, or composite nanofluids. These advanced nanofluids integrate the chemical and physical properties of the suspended nanoparticles within a single phase, yielding diverse effects from the combined elements [3]. Babu et al. [4] found that hybrid nanomaterials display distinct physicochemical characteristics absent in general fluids or mono nanofluids. This discovery spurred further research on various hybrid nanofluids, examining their preparation, synthesis, and characterization stages. It was reported that thermal conductivity in hybrid nanofluids surpassed that of mono nanofluids [5]. In addition, hybrid nanofluids achieved higher heat flux than mono nanofluids in a study of Copper-Alumina/water (Cu-Al_2O_3/H_2O) by Nadeem et al. [6]. Salah et al. [7] reported that using the Al-Mg-TiO_2/water-ethylene glycol ternary hybrid nanofluid substantially increases the heat transfer coefficient for swirl flow within a rotating cone.

Blood is considered an incompressible flow consisting of the boundary layer flow and the potential flow within arteries. Analyzing blood flow over cylindrical surfaces has crucial applications in diagnosing and treating conditions related to plaque deposition and aneurysms in cardiovascular diseases, minimizing post-operative complications, and reducing healthcare costs. This analysis also applies to tumor treatments, blood clot removals, brain aneurysms, and infections. However, selecting appropriate models and approaches to depict blood flow challenges is vital to ensure realistic and effective solutions. According to Akhtar et al. [8], many researchers preferred non-Newtonian boundary layer models to study arterial blood flows, as these models provide a more accurate representation of hemodynamics. Recent studies have also reported on blood nanofluid boundary layer flows. Akhtar et al. [8] simulated blood flow within a symmetrically stenosed artery using the non-Newtonian Casson model, suggesting that their findings are crucial for surgical considerations, including assessing stenosis shape, location, and formation. McCash et al. [9] numerically explored the entropy analysis of the peristaltic flow of a Cu-Ag/water hybrid nanofluid within an elliptical duct with sinusoidal progressing boundaries. Tripathi et al. [10] presented a theoretical and numerical evaluation of unsteady blood flow in a diseased artery featuring irregular stenosis, focusing on drug delivery applications for blood vessels using an Ag-gold/blood hybrid nanofluid boundary layer model. Sharma et al. [11] examined the impact of the Au-Al_2O_3/blood hybrid nanoliquid on the hemodynamic properties of unsteady blood flow in a curved artery with stenosis and aneurysm. They concluded that the chosen hybrid nanomaterials can modulate blood velocity and temperature, enabling surgeons to adjust them as required.

Sutterby liquid is crucial in the polymer industry, making it one of the most frequently discussed non-Newtonian fluids due to its rheological features [12]. This non-Newtonian fluid model characterizes the behavior of pseudoplastic substances. To date, researchers have presented their findings using both analytical and numerical methods across various geometries to evaluate the heat energy efficiency of non-Newtonian Sutterby hybrid nanofluid flows. Waqas et al. [13] studied SiO_2-SWCNT/EG and MoS_2-MWCNT/EG hybrid nanofluid boundary layer flows in the three-dimensional Sutterby model over a stretchy surface affected by thermal convection, radiation, and heat melting. They observed that the temperature and velocity profiles decrease when larger melting parameter values are applied. Al-Mughanam et al. [14] numerically examined the characteristics of mono, duo, and tri-nanoparticles suspended in the Sutterby fluid model using the Finite Element Method (FEM). They noted moderate values of thermal memory effects in the hybrid nanofluid compared to other types of nanofluids under consideration. Bouslimi et al. [15] discussed the heat transport efficiency of Sutterby mono and hybrid nanofluid flows past a slippery hot surface, while Jamshed et al. [16] found in their study that Sutterby nanofluids using hybrid Copper-Sodium-Alginate (Cu-SA) and Gold-Sodium-Alginate (Au-SA) nanoparticles enhance the rate of heat transfer in the Parabolic Trough Solar Collector (PSTC). These studies highlight that non-Newtonian Sutterby fluids have found use in various applications, including lubrication and drilling operations.

The importance of nanoliquids by focusing on the solid nanoparticles' volume fraction, where the thermophysical properties of both the base fluid and nanoparticles are heterogeneously correlated, was initially examined by Tiwari et al. [17]. Numerous studies on the Tiwari and Das hybrid nanofluid models are now available in the literature. Dinarvand et al. [18] analytically explored the Cu-Ag/water hybrid nanoliquid model developed based on the Tiwari–Das framework near a vertically permeable circular channel. A subsequent study by Dinarvand et al. [19] found that the Tiwari-Das Falkner-Skan model for TiO_2-CuO/water hybrid nanofluids outperforms mono-nanofluids regarding heat flux. Additionally, Ramzan et al. [20] utilized the Tiwari-Das model for SiO_2-TiO_2/water hybrid nanofluid flows through a rotary channel influenced by the Hall current. They indicated that the hybrid nanofluid flow is superior to the performance of mono-nanofluid systems in solar thermal applications. Alwawi et al. [21] developed the Tiwari-Das mathematical model to simulate the behavior of Williamson hybrid nanoliquid flows over a cylinder. They reported that silver-aluminum oxide nanoparticles demonstrate superiority in enhancing the velocity and energy transfer of the base fluid. Furthermore, Saranya et al. [22] examined the thermal behavior of the Blasius-Sakiadis Tiwari-Das flow for water-based ternary hybrid nanofluids, considering the effect of nanoparticle shape.

The attention focused on selecting various types of graphene-based solid nanoparticles for producing single and hybrid nanoliquids offers significant advantages for technological and scientific approaches. Graphene-based nanoparticles provide excellent thermal conductivity and stability and serve as flexible transporters with minimal corrosion and erosion [23]. Moreover, because graphene-based materials exhibit superior electrical conductivity, high chemical stability, and exceptional mechanical behavior, they are efficiently utilized in supercapacitors and other energy storage devices [24]. Graphene-based materials have also demonstrated vast applicability in the medical field for applications such as cancer therapy and diagnosis, sensing and imaging, tissue regeneration, and drug delivery [25]. Mehrali et al. [26] reported that graphene-magnetite hybrid nanoparticles increase the fluid thermal conductivity by approximately 11%. In contrast, Sadeghinezhad et al. [27] observed that graphene nanoparticles offer higher stability and a surface area thousands of times greater than other nanoparticles. Additionally, Purbia et al. [28] reported that the heat flux increases by about 32% at a 0.1% concentration of graphene nanomaterials, attributed to the enhanced thermal conductivity and Reynolds number of the conducting solid nanomaterials. Bouslimi et al. [15] also found that the thermal transmission rate of the Sutterby hybrid Cu-GO/engine oil nanoliquid surpasses that of the mono Cu/engine oil nanoliquid.

Limited studies on the Sutterby liquid model over a cylinder inspired the current research to further investigate the heat flux efficiency of selected hybrid nanofluids. The examination of graphene, graphene oxides (GO), and graphene nanoplatelets (GNP) as potential nanomaterials in fluid mechanics remains infrequent despite their exceptional combination of mechanical and electrical properties. This research is the first to analyze graphene, GO, and GNP nanoparticles dispersed in the radiative Cu/blood mono nanofluid to form various hybrid mixtures around a slanted permeable cylinder in the existing literature. The impacts of thermal radiation and the heat source are also considered in this study. MATLAB's bvp4c code is utilized to address the transformed boundary value problems derived from the primary set of partial differential equations (PDEs). Comprehensive results are validated and compared, and the effects of specific parameters on the hybrid Sutterby non-Newtonian nanofluids in terms of non-dimensional velocity and temperature distributions, reduced skin friction value, and reduced Nusselt number are thoroughly investigated. The findings are then presented in tables and graphs in the final section of this research.

Accordingly, the contributions of this research are outlined as follows:

1. This study represents the first exploration of the non-Newtonian Sutterby Tiwari-Das model using blood as the base fluid with hybrid nanoparticles, while previous research focused on other conventional base fluids [15,16].
2. The dispersion of various graphene, GO, and GNP nanoparticles in the radiative Cu/blood mixture is theoretically conducted for the first time to formulate hybrid nanofluid models.
3. Thermal radiation and the effects of the heat source are incorporated into this expanded model alongside a slanted permeable cylinder.

2 Mathematical Modelling

In the current research, a non-Newtonian Sutterby fluid model over a leaning permeable cylinder is given due consideration. The stress tensor is specified as [15]:

$$T = -Ip + S, \tag{1}$$

where I and p express identity-tensor and pressure, respectively, while S implies an additional stress-tensor, which is defined as follows:

$$S = A_1 \left[\frac{\sinh^{-1}(\dot{\gamma} E)}{\dot{\gamma} E} \right]^{\chi} \mu_0, \tag{2}$$

with E and μ_0 are designated as material time-constant and zero-shear rate of viscosity, respectively. The first term of Eq. (1) indicates the element of viscoelasticity. Moreover, the fluid reflects the Newtonian behavior when $\chi = 0$, the fluid becomes pseudoplastic (shear-thinning) when $\chi > 0$, and the fluid serves as dilatant (shear-thickening) when $\chi < 0$. Accordingly, the Rivlin-Ericksen tensor of first-order, A_1 and the second invariant strain tensor, $\dot{\gamma}$ are expressed as follows:

$$A_1 = (\text{grad } V) + (\text{grad } V)^{\mathrm{T}}, \tag{3}$$

$$\dot{\gamma} = \sqrt{\frac{\mathrm{tr}\,(A_1)^2}{2}}. \tag{4}$$

The viscosity of blood varies with shear rate and is determined by several factors, such as the viscosity of plasma, blood cell distribution, and the mechanical properties of the blood cells. Due to their high concentration and distinct mechanical properties, most non-Newtonian effects originate from red blood cells. As blood exhibits non-Newtonian properties of shear-thinning and viscoelasticity, the present research uses the Sutterby model to represent a steady, incompressible, laminar, non-Newtonian blood fluid flow.

The base blood fluid is initially mixed with copper nanoparticles to form Cu/blood mono nanofluids using the Tiwari-Das hybrid nanofluid model. Subsequently, hybrid nanofluids are fabricated by dispersing three types of selected nanoparticles (graphene, GO, and GNP). Table 1 presents the existing models of mono and hybrid nanofluids' thermophysical properties [18]. Similarly, quantities from references [12,18,29,30] for the base fluid and selected nanoparticles for this study are provided in Table 2. The velocity of the mainstream flow over the cylindrical coordinates (x, r) is assumed to be $U(x) = U_0 (x/l)$. The thermal radiation and source of heating effect are also considered. The thermal radiation and heating effects are considered. The geometry of the hybrid nanofluid flow over a slanted permeable cylinder with radius R is depicted in Fig. 1.

Table 1: Existing models for mono and hybrid nanofluids [18]

Properties	Mono nanofluid	Hybrid nanofluid
Viscosity, μ	$\dfrac{\mu_f}{(1-\phi_1)^{2.5}}$	$\dfrac{\mu_f}{(1-\phi_1)^{2.5}(1-\phi_2)^{2.5}}$
Kinematic viscosity, ν	$\dfrac{\mu_{nf}}{\rho_{nf}}$	$\dfrac{\mu_{hnf}}{\rho_{hnf}}$

(Continued)

Table 1 (continued)

Properties	Mono nanofluid	Hybrid nanofluid
Density, ρ	$\phi_1\rho_{s1}+\rho_f(1-\phi_1)$	$\phi_2\rho_{s2}+[\{(1-\phi_1)\rho_f+\phi_1\rho_{s1}\}(1-\phi_2)]$
Capacity of heat, ρC_p	$\phi_1\left(\rho C_p\right)_{s1}+\left(\rho C_p\right)_f(1-\phi_1)$	$\phi_2\left(\rho C_p\right)_{s2}+\left[\left\{(1-\phi_1)\left(\rho C_p\right)_f+\phi_1\left(\rho C_p\right)_{s1}\right\}(1-\phi_2)\right]$
Diffusivity, α	$\frac{k_{nf}}{\left(\rho C_p\right)_{nf}}$	$\frac{k_{hnf}}{\left(\rho C_p\right)_{hnf}}$
Thermal conductivity, k	$k_f\left[\frac{(n-1)k_f+k_{s1}-\left(k_f-k_{s1}\right)(n-1)\phi_1}{(n-1)k_f+k_{s1}+\left(k_f-k_{s1}\right)\phi_1}\right]$	$k_f\left[\frac{(n-1)k_{nf}+k_{s2}-\left(k_{nf}-k_{s2}\right)(n-1)\phi_2}{(n-1)k_{nf}+k_{s2}+\left(k_{nf}-k_{s2}\right)\phi_2}\right]\left[\frac{(n-1)k_f+k_{s1}-\left(k_f-k_{s1}\right)(n-1)\phi_1}{(n-1)k_f+k_{s1}+\left(k_f-k_{s1}\right)\phi_1}\right]$

Table 2: Base fluid's and selected nanoparticles' thermophysical properties [12,18,29,30]

Thermophysical properties	Blood [12]	Cu [18]	Graphene [29]	GO [12]	GNP [30]
ρ $\left(\mathrm{kg/m^3}\right)$	1060	8933	2250	1800	2100
C_p (J/kgK)	3770	385	2100	2510	1200
k (W/mK)	0.5401	400	2500	5000	4000
n [31]		3	3	3	5.7

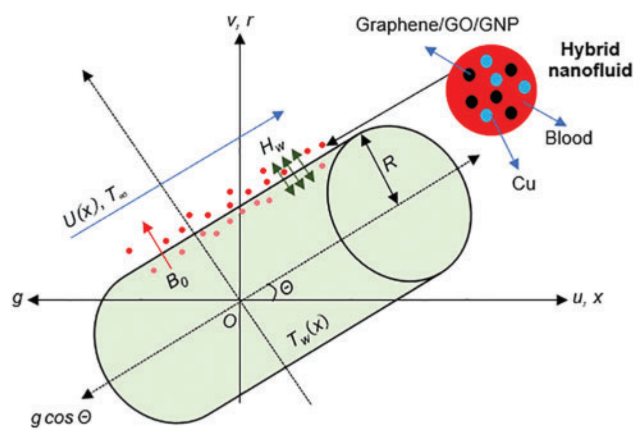

Figure 1: Schematic diagram of the flow with geometrical coordinates

The governed PDEs of continuity, momentum, and energy, as referenced in [15,18,29] with the corresponding boundary conditions (BCs), are given as:

$$\frac{\partial u}{\partial x}(r)+\frac{\partial v}{\partial r}(r)=0, \tag{5}$$

$$\frac{\partial u}{\partial x}(u)+\frac{\partial u}{\partial r}(v)=\nu_{hnf}\frac{1}{2}\frac{\partial^2 u}{\partial r^2}\left(1-\frac{mb^2}{2}\left(\frac{\partial u}{\partial r}\right)^2\right)+\frac{\sigma B_0{}^2}{\rho_{hnf}}\mathrm{u}+\frac{(\rho\beta_T)_{hnf}}{\rho_{hnf}}(T-T_\infty)\,g\cos\Theta, \tag{6}$$

$$\left(\rho c_{\mathrm{p}}\right)_{hnf}\left(\frac{\partial T}{\partial x}(u)+\frac{\partial T}{\partial r}(v)\right)=k_{hnf}\left(\frac{\partial^2 T}{\partial r^2}+\frac{1}{r}\frac{\partial T}{\partial r}\right)+\frac{16\sigma^* T_\infty^3}{3\,k^*}\frac{\partial^2 T}{\partial r^2}+Q^*(T-T_\infty), \tag{7}$$

$$\left.\begin{array}{l} u=U(x),\quad v=H_{w*},\quad T=T_w \text{ at } r=R, \\ u\to 0,\quad T\to T_\infty \text{ as } r\to\infty, \end{array}\right\}, \tag{8}$$

For these, two cases of suction $(H_{w*}<0)$ and injection $(H_{w*}>0)$ are considered. Subsequent similarity transformations are presented as follows:

$$\left.\begin{array}{l} u=U_0\left(\dfrac{x}{l}\right)f'(\eta),\quad v=-\dfrac{R}{r}\left(\dfrac{U_0\nu_f}{l}\right)^{\frac{1}{2}}f(\eta),\ \eta=\dfrac{r^2-R^2}{2R}\left(\dfrac{U_0}{\nu_f l}\right)^{\frac{1}{2}}, \\ \psi=\left(\dfrac{U_0\nu_f\,x^2}{l}\right)^{\frac{1}{2}}Rf(\eta),\ \theta(\eta)=\dfrac{T-T_\infty}{T_w-T_\infty} \end{array}\right\}, \tag{9}$$

with ψ as the stream function, is characterized in $u=r^{-1}(\partial\psi/\partial r)$ and $v=-r^{-1}(\partial\psi/\partial r)$.

By substituting Eq. (9) into Eqs. (6) and (7), a dimensionless system of nonlinear ODEs is derived as below:

$$2\frac{G_0}{G_1}\left((1+2\gamma\eta)f'''-\frac{1}{2}(1+2\gamma\eta)^2\sigma f''^2 f'''\right)+\frac{M}{G_1}f'\frac{G_2}{G_1}\lambda\cos\Theta-f'^2+f''f=0, \tag{10}$$

$$(G_4+Rd)(1+2\gamma\eta)\theta''+(2G_4+Rd)\gamma\theta'+G_3 Pr\,f\,\theta'+PrQ\theta=0, \tag{11}$$

where

$$G_0=(1-\phi_1)^{2.5}(1-\phi_2)^{2.5},\ G_1=(1-(\phi_1+\phi_2))+\phi_1\frac{\rho_{s_1}}{\rho_f}+\phi_2\frac{\rho_{s_2}}{\rho_f},$$

$$G_2=(1-(\phi_1+\phi_2))+\phi_1\frac{(\rho\beta_{\mathrm{T}})_{s_1}}{(\rho\beta_T)_f}+\phi_2\frac{(\rho\beta_T)_{s_2}}{(\rho\beta_T)_f},$$

$$G_3=(1-(\phi_1+\phi_2))+\phi_1\frac{\left(\rho c_p\right)_{s_1}}{\left(\rho c_p\right)_f}+\phi_2\frac{\left(\rho c_p\right)_{s_2}}{\left(\rho c_p\right)_f},$$

$$G_4=\left[\frac{2\kappa_f+\dfrac{\left(\phi_1\kappa_{s_1}+\phi_2\kappa_{s_2}\right)}{\phi_1+\phi_2}+2\left(\phi_1\kappa_{s_1}+\phi_2\kappa_{s_2}\right)-2\kappa_f(\phi_1+\phi_2)}{2\kappa_f+\dfrac{\left(\phi_1\kappa_{s_1}+\phi_2\kappa_{s_2}\right)}{\phi_1+\phi_2}+\left(\phi_1\kappa_{s_1}+\phi_2\kappa_{s_2}\right)-\kappa_f(\phi_1+\phi_2)}\right], \tag{12}$$

These equations depend on the BCs:

$$\left.\begin{array}{l} f(\eta)=H_w,\ f'(\eta)=1,\ \theta(\eta)=1 \text{ at } \eta=0, \\ f'(\eta)\to 0,\ \theta(\eta)\to 0 \text{ as } \eta\to\infty. \end{array}\right\}, \tag{13}$$

f and θ are individual functions related to the dimensionless velocity and temperature profiles for the examined hybrid nanoliquids, and primes denote differentiation with respect to η.

The selected parameters used in this problem are defined mathematically as follows:

$$\gamma=\frac{1}{R}\left(\frac{\nu_f l}{U_0}\right)^{\frac{1}{2}},\ \sigma=\frac{mb^2U_0^3x^2}{\nu_f l^3},\ M=\frac{\sigma B_0^2 1}{\rho_f U_0},\ \lambda=\frac{Gr_x}{Re_x^2},\ Pr=\frac{\left(\mu c_p\right)_f}{\kappa_f},$$

$$Rd = \frac{4\sigma^* T_\infty{}^3}{\kappa_f k^*},\ H_w = -\frac{r}{R}\left(\frac{l}{v_f U_0}\right)^{\frac{1}{2}} H_w^*,\ Q = \frac{Q^*}{U_0 \left(\rho C_p\right)_f},\ Re = \frac{U_0 l}{v_f}. \tag{14}$$

The skin friction, C_f and Nusselt number, Nu_x are substantial quantities describing the fluid flow and are defined in [10].

$$C_f = \frac{\tau_w}{\rho_f U_0{}^2},\quad Nu_x = \frac{x q_w}{\kappa_f \left(T_w - T_\infty\right)}, \tag{15}$$

where τ_w and q_w are described as:

$$\tau_w = \mu_{hnf}\left(\frac{\partial u}{\partial r} + \frac{mb^2}{3}\left(\frac{\partial u}{\partial r}\right)^3\right)_{r=R},\quad q_w = -\kappa_{hnf}\left(1 + \frac{16\sigma^* T_\infty^3}{3k^* v_f \left(\rho C_p\right)_f}\frac{\partial T}{\partial r}\right)_{r=R}. \tag{16}$$

When Eq. (9) is substituted into Eq. (14), the resulting reduced skin friction and reduced Nusselt number are obtained:

$$C_f\ Re^{\frac{1}{2}} = \frac{1}{G_0}\left(f''(\eta) + \frac{\sigma}{3} f''(\eta)^3\right),\ Nu_x Re^{-\frac{1}{2}} = -\frac{\kappa_{hnf}}{\kappa_f}(1 + Rd)\,\theta'\eta. \tag{17}$$

3 Methods

In order to address the mathematical model for this problem, a robust solution technique is needed to ensure the accuracy and reliability of the outcomes of the controlling PDEs. Therefore, the numerical procedure for this non-Newtonian Sutterby hybrid nanoliquid flow of Cu-blood with chosen graphene, GO, or GNP over a slanted permeable cylinder is conducted using the bvp4c package in MATLAB. The bvp4c tool, derived from the finite difference technique, uses the collocation process in the Lobatto IIIa [32] formula. Additionally, the package implements a derivative scheme in the form of f' based on the initial solution estimates and BCs [33]. This approach offers a straightforward algorithm with reduced cost and high computational speed compared to other methods. Furthermore, many researchers have utilized this code, validating it as an effective solution for various mathematical and engineering challenges.

Given the variables:

$$\left.\begin{array}{l} f = F_{(1)},\quad f' = \dfrac{\partial F_{(1)}}{\partial \eta} = F_{(2)},\quad f'' = \dfrac{\partial F_{(2)}}{\partial \eta} = F_{(3)}, \\ f''' = \dfrac{\partial F_{(3)}}{\partial \eta},\ \theta = F_{(4)},\ \theta' = \dfrac{\partial F_{(4)}}{\partial \eta} = F_{(5)}, \\ \theta'' = \dfrac{\partial F_{(5)}}{\partial \eta}, \end{array}\right\}, \tag{18}$$

a shooting approach is employed to reformulate the nonlinear Eqs. (10) and (11) with the BCs (13). The equations are decreased into the first-order DEs as follows:

$$F'_{(3)} = \frac{1}{2\left((1+2\gamma\eta) - \frac{1}{2}(1+2\gamma\eta)^2 \sigma F_{(3)}{}^2\right)}\left(\frac{G_1}{G_0}\right)\left[F_{(2)}{}^2 - F_{(3)}F_{(1)} - \frac{M}{G_1}F_{(2)} - \frac{G_2}{G_1}\lambda\cos\Theta\right], \tag{19}$$

$$F'_{(5)} = -\frac{1}{(G_4 + Rd)(1+2\gamma\eta)}\left[(2G_4 + Rd)\,\gamma F_{(5)} + G_3 Pr F_{(1)} F_{(5)} + PrQF_{(4)}\right]. \tag{20}$$

Thus, the boundary conditions are defined as follows:

$$\left.\begin{array}{l} F_{(1)} = H_w,\ F_{(2)} = 1,\ F_{(4)} = 1 \text{ at } \eta = 0, \\ F_{(2)} \to 0,\quad F_{(4)} \to 0 \text{ as } \eta \to \infty. \end{array}\right\}. \tag{21}$$

$F_{(3)}$ and $F_{(5)}$ are assumed to have initial values of 0 and the preferred limits for η range from 0 to 10. In addition, the problem is also solved with a residual tolerance of 10^{-6}.

4 Results and Discussion

The range of selected nanoparticles' volume fraction for ϕ_1 and ϕ_2 is from 0 to 0.04, which is simulated for the current problem. All calculations consider the specific shape factor of the nanoparticles, as listed in Table 2. Moreover, the Prandtl number, $\mathrm{Pr} = 19.4049$ [12] is utilized to represent the blood fluid. The distributions of velocity, temperature, reduced skin friction value, and reduced Nusselt number for various parameters, including curvature parameter γ, Sutterby fluid parameter ζ, Hartmann number M, mixed convection λ, angle of inclination Θ, thermal radiation Rd, wall permeability parameter H_w and local source of heating parameter Q are presented in figures and tables for clarity. The applied range of parameter values is given in Table 3.

Table 3: The applied ranges of the emerging parameters for the current study

Emerging parameters	Ranges
γ	$0 \le \gamma \le 3$
ζ	$0.2 \le \zeta \le 0.8$
M	$0.1 \le M \le 0.4$
λ	$0 \le \lambda \le 0.3$
Θ	$0 \le \Theta \le 90$
Rd	$4 \le Rd \le 7$
H_w	$-1 \le H_w \le 1$
Q	$0.1 \le Q \le 0.4$
$\phi_1,\ \phi_2$	$0 \le \phi_1,\ \phi_2 \le 0.04$

4.1 Validations

For the purpose of validation, the current results of the bvp4c code for Cu-water mono nanofluid are compared with the outcomes of previous work [18]. The comparison in Table 4 supports the conclusions drawn from the present study.

Table 4: Comparison between present and previous [18] outcomes on the effects of λ and ϕ_1 on Cu-water mono nanofluid when $Pr = 6.2$, $\gamma = 1$, $\phi_2 = 0$, $M = 0$ and $H_w = 0$

λ	ϕ_1	$C_f\ Re^{1/2}$		$Nu_x Re^{-1/2}$	
		[18]	Present	[18]	Present
0	0.0	1.71067	1.72103	2.15300	2.15401
	0.1	2.51318	2.51415	2.69711	2.69715
	0.2	3.46936	3.47009	3.26987	3.27002

(Continued)

Table 4 (continued)

λ	ϕ_1	$C_f\ Re^{1/2}$		$Nu_x Re^{-1/2}$	
		[18]	Present	[18]	Present
5	0.0	3.02257	3.02231	2.41023	2.41035
	0.1	3.83694	3.83612	2.92326	2.92332
	0.2	4.84887	4.85097	3.47738	3.47720

4.2 Velocity and Temperature Disseminations

In this section, the velocity and temperature distributions are thoroughly analyzed. Fig. 2 illustrates the effects of ϕ_2 on these distributions. The values of ϕ_2 range from 0 to 0.04 for graphene, GO, and GNP and are combined with Cu ($\phi_1 =$ 0.02)/blood to form hybrid nanofluids. Fig. 2a indicates that velocity profiles decrease for all types of hybrid nanofluids with increasing values of ϕ_2. From the figure, Cu-blood mono nanofluids ($\phi_2 = 0$) demonstrate the highest velocity distribution compared to other hybrid nanofluids. Conversely, Fig. 2b displays the rise in temperature distribution with increasing ϕ_2. Cu-graphene/blood hybrid nanofluids exhibit the highest velocity but the lowest temperature distribution, while Cu-GNP/blood hybrid nanofluids present the opposite. Both graphene and GO nanoparticles are spherical ($n = 3$), while GNPs are nanoplatelets ($n = 5.7$) with a larger nanoparticle surface area than spheres. Greater nanoparticle volume fractions in hybrid blood flows ($\phi_2 \neq 0$) and larger nanoparticle surface areas in contact with the cylindrical surface increase friction on the cylindrical surface. Consequently, velocities decrease, and temperatures rise in the nanofluid flows. This pattern can explain the observations in Fig. 2.

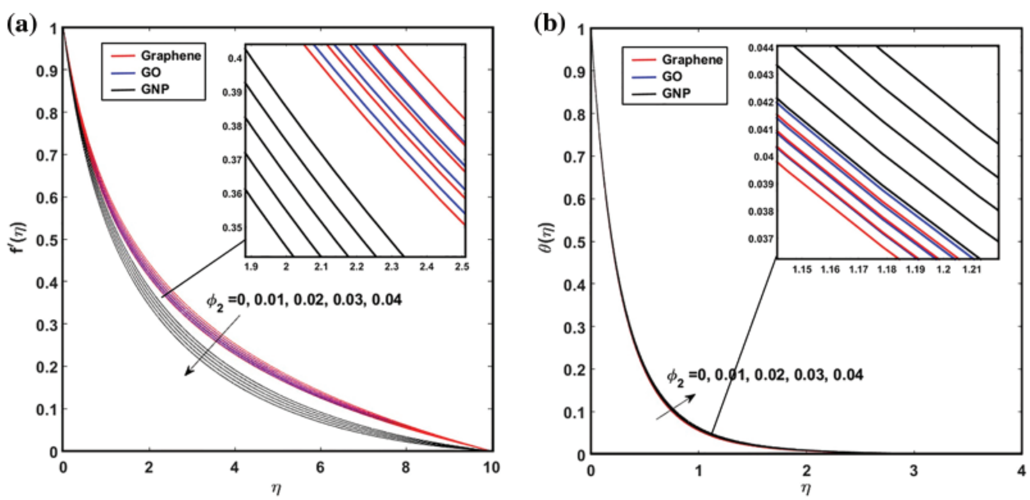

Figure 2: The repercussion of ϕ_2 on (a) velocity and (b) temperature distributions

Fig. 3 elucidates the effects of Θ on velocity and temperature distributions as inclination angles increase from 0° to 90°. Figs. 3a and 3b indicate that the distributions reach their peak and trough at $\Theta = 0°$, respectively. In contrast, the distributions are at their minimum and maximum at $\Theta = 65°$, respectively. Cu-GO/blood hybrid nanofluid has the highest velocity distribution at $\Theta = 0°$, while Cu-GNP/blood hybrid nanofluid has the highest temperature distribution at $\Theta = 65°$. Conversely, the opposite effects are observed for velocity and temperature distributions of Cu-GO/blood hybrid nanofluid at $\Theta = 65°$ and $\Theta = 0°$, respectively. Irregular patterns in flow velocity and temperature remain unclear. However, when the cylinder is inclined or vertical ($\Theta > 0°$), the flow direction is hindered by both gravity and surface friction, reducing velocity and increasing temperature due to added resistances to nanofluid movement.

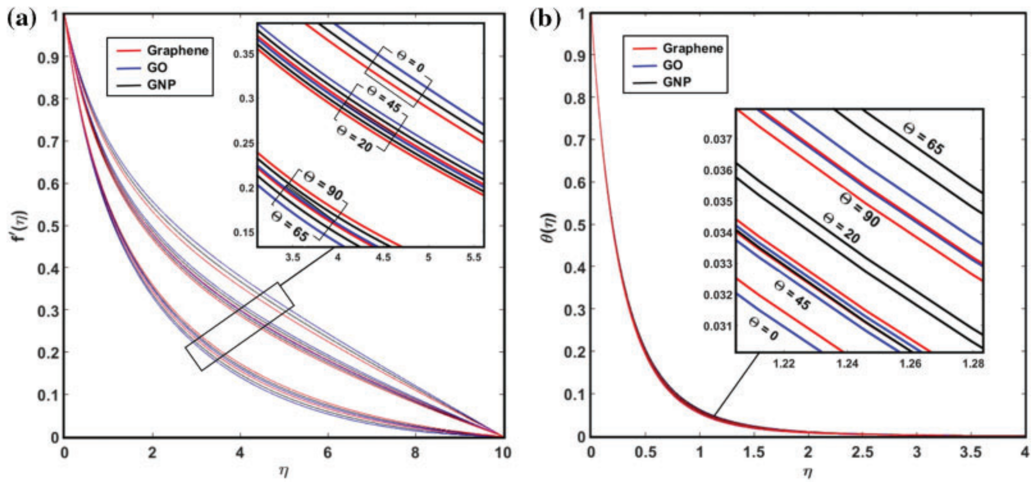

Figure 3: The repercussion of Θ on (a) velocity and (b) temperature distributions

Fig. 4 illustrates the influences of γ, ζ, M, λ and H_w on the velocity distributions. Fig. 4a depicts the velocity distribution increase for greater values of γ. As γ increases, the radius of the cylinder shortens, and consequently, the acceleration of the fluid flow intensifies due to the reduced flow resistance. Notably, the wall surface resembles a flat surface when $\gamma = 0$. According to Fig. 4a, Cu-GO/blood hybrid nanofluids display the highest velocity distribution when γ ranges from 0 to 3. Conversely, Fig. 4b indicates that velocity decreases as values of ζ increase. The velocity distributions for Cu-GO/blood hybrid nanofluids peak when σ ranges from 0.2 to 0.8. Fig. 4c reveals a speed inclination for higher M values of M. The results show that Cu-GO/blood hybrid nanofluids achieve the highest velocity when M ranges from 0.1 to 0.4. This phenomenon results from the increase of the Lorentz drag force, which hinders the flow movement and increases the temperature of the nanofluids.

Alternatively, Figs. 4d and 4e demonstrate that the velocity distributions decline as the values of the mixed convection parameter, λ and the wall permeability parameter, H_w, increase. It indicates that all chosen hybrid nanofluids attain the highest velocity distributions at $\lambda = 0$, while Cu-GO/blood hybrid nanofluid has the lowest velocity distribution at $\lambda = 0.3$ (Fig. 4d). Notably, the cylinder wall is impermeable when $H_w = 0$, whereas $H_w > 0$ represents an injection case, and $H_w < 0$ corresponds to a suction case. In Fig. 4e, Cu-GNP/blood hybrid nanofluid displays the lowest velocity profile for $H_w = 1$, while both Cu-GO/blood and Cu-graphene/blood hybrid nanofluids exhibit the highest velocity distributions at $H_w = -1$. When the wall undergoes injection ($H_w = 1$), it creates resistance and amplifies the opposing force in the flow direction. The increased nanoparticle surface area in contact with the cylindrical surface impedes the flow velocity distribution. From Fig. 4, Cu-GO/blood and subsequently Cu-graphene/blood hybrid nanofluids consistently present the maximum velocity distributions. In contrast, Cu-GNP/blood hybrid nanofluid consistently has the minimum velocity distribution for all γ, ζ, M, and H_w parameters, except for the λ parameter.

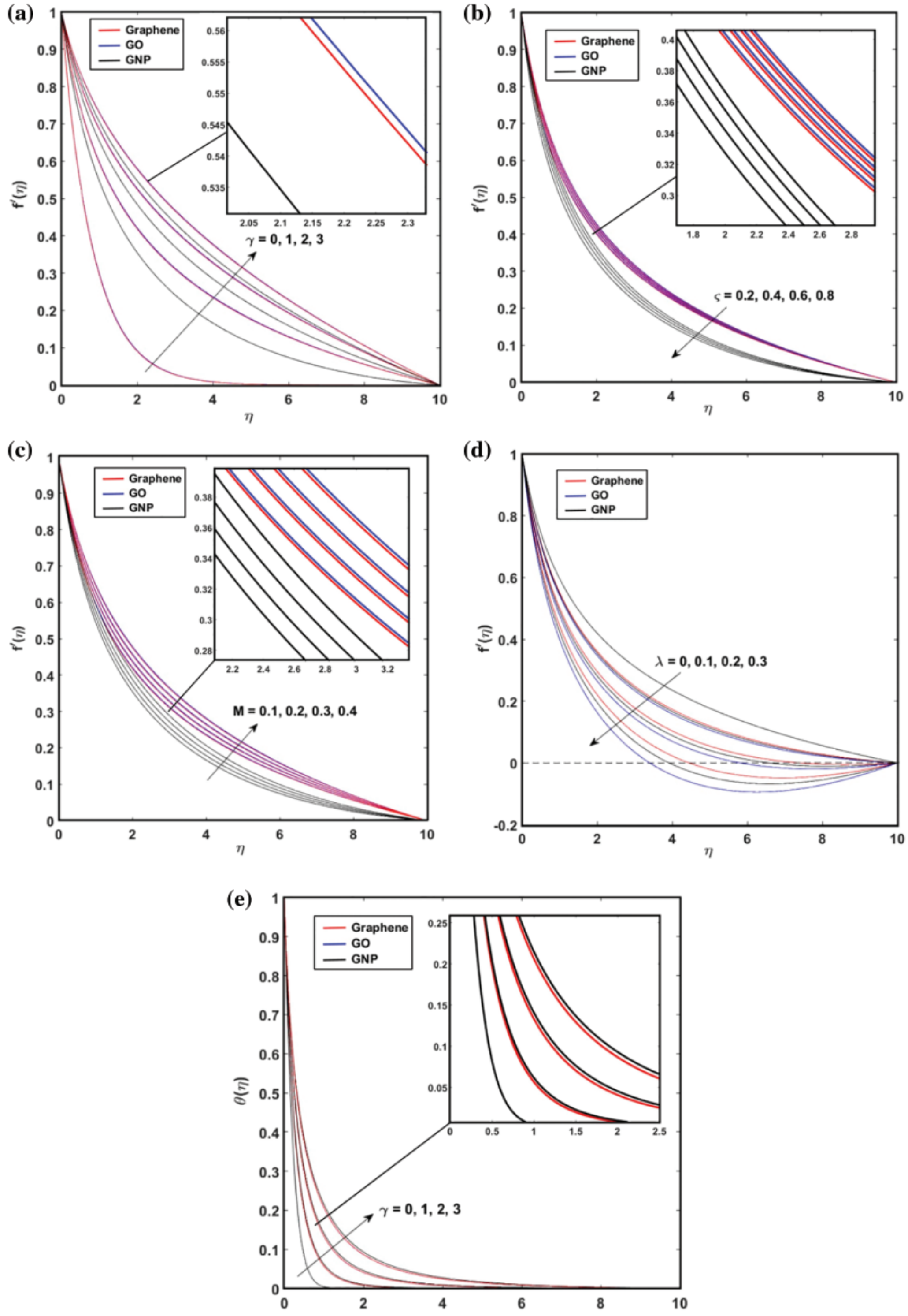

Figure 4: The repercussions of (a) γ, (b) ζ, (c) M, (d) λ and (e) H_w on velocity distributions

The influences of γ, ζ, M, λ, Rd, H_w, and Q on the temperature distribution are discussed in Fig. 5. Figs. 5a and 5b show the increase in temperature distributions with increasing values of γ from 0 to 3 and ζ from 0.2 to 0.8, respectively. The temperature distribution is lowest for all selected hybrid nanofluids when $\gamma = 0$, but the Cu-GNP/blood hybrid nanofluid exhibits the highest temperature distribution when $\gamma = 3$, as seen in Fig. 5a. Fig. 5b reveals that Cu-GNP/blood hybrid nanofluids possess the highest temperature distribution, while Cu-GO/blood hybrid nanofluids have the lowest for all values of ζ used in this study. In addition, Fig. 5c demonstrates a decline in temperature distributions with increasing values of M from 0.1 to 0.4. It also emphasizes that Cu-GNP/blood hybrid nanofluids consistently maintain the highest temperature distribution. In contrast, Cu-GO/blood hybrid nanofluids are at the lowest for all examined values of M. Fig. 5d highlights an incline in temperature distributions as λ increases from 0 to 0.3. All chosen hybrid nanofluids have their lowest temperature distribution at $\lambda = 0$, while Cu-GO/blood hybrid nanofluids attain the highest velocity temperature at $\lambda = 0.3$. The velocity distribution also increases, as shown in Fig. 5e, with greater values of Rd. The thermal gradient rises, and the mean absorption coefficient decreases with increasing Rd. As a result, the temperature distribution elevates with higher levels of thermal radiation. Fig. 5e shows that Cu-GNP/blood hybrid nanofluids lead in temperature distribution, followed by Cu-graphene/blood and Cu-GO/blood hybrid nanofluids for all Rd values ranging from 4 to 7. Furthermore, Fig. 5f illustrates a decrease in temperature distribution as H_w values rise from -1 to 1. However, a consistent observation from this figure is that Cu-GNP/blood hybrid nanofluids still have the highest temperature distribution, followed by Cu-graphene/blood and Cu-GO/blood hybrid nanofluids for all H_w values. Fig. 5f demonstrates an increase in temperature distribution for rising Q values from 0.1 to 0.4 across all hybrid nanofluids. In summarizing the results from Fig. 5, Cu-GNP/blood hybrid nanofluids consistently have the highest temperature distribution, followed by Cu-graphene/blood and Cu-GO/blood hybrid nanofluids for the γ, ζ, M, Rd, H_w,” and Q parameters, except in the case of the mixed convection parameter, λ.

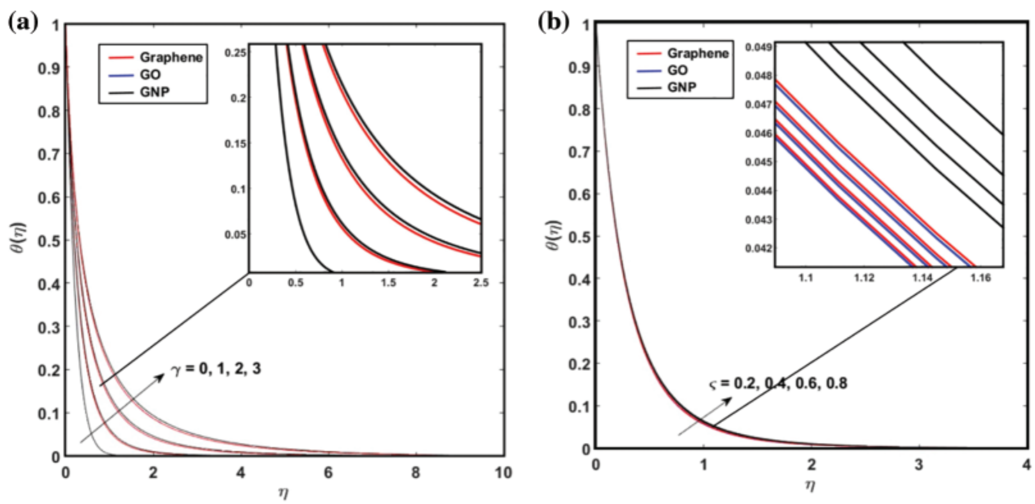

Figure 5: (Continued)

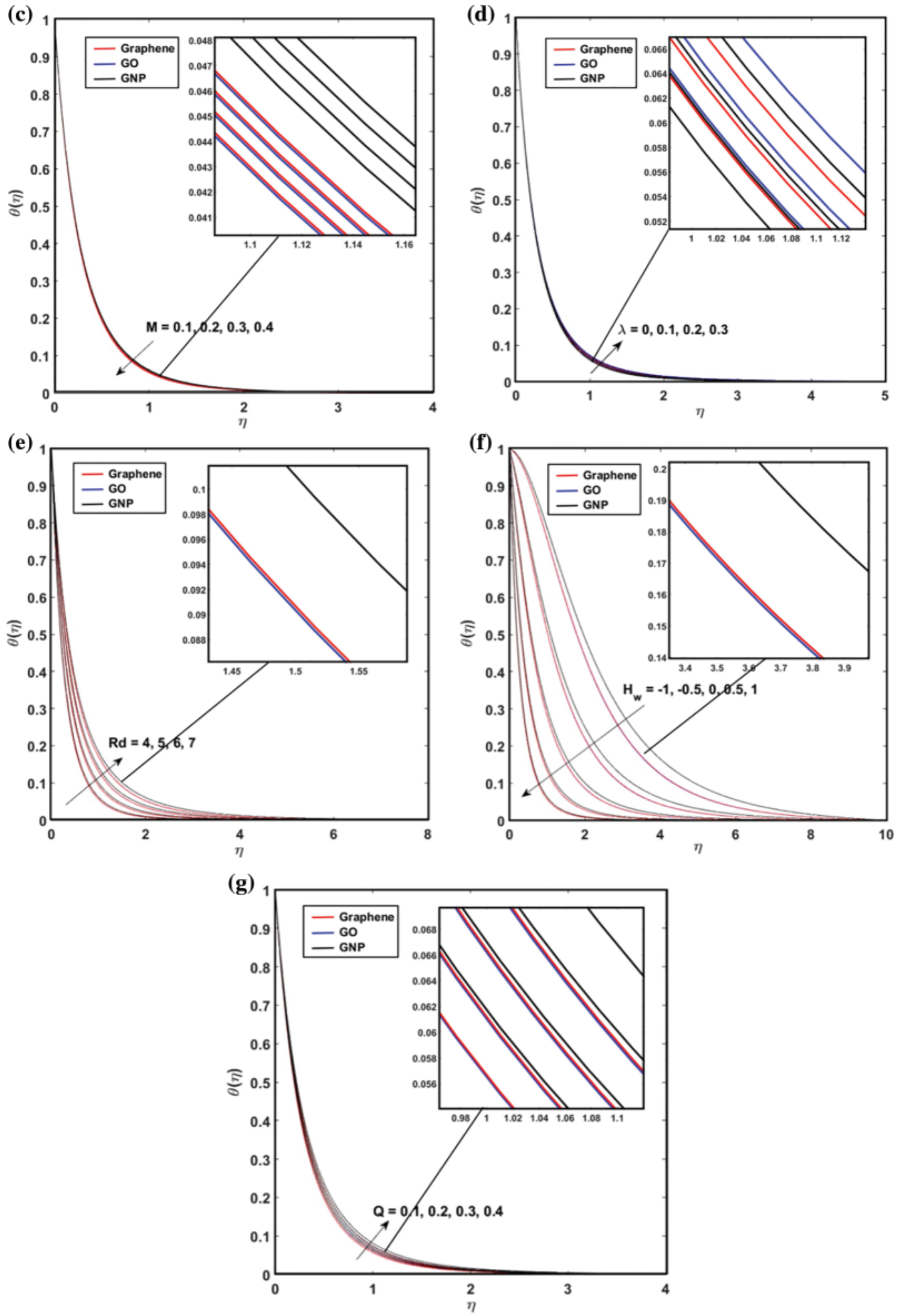

Figure 5: The repercussion of (a) γ, (b) ζ, (c) M, (d) λ, (e) Rd, (f) H_w and (g) Q on temperature distributions

4.3 Reduced Skin Friction Value and Reduced Nusselt Number

This section particularly interprets and explains the outcomes of reduced skin friction value and reduced Nusselt number. It is important to note that negative signs for the values of reduced skin friction generated from this present study represent the magnitude in which it shows the friction is opposite to the direction of the flow. The impacts of Θ on the two quantities are presented in Table 5. The values of Θ from 0° to 90° are implemented in the present study in which the value of $\Theta = 0°$ indicates that the cylinder is at the horizontal position while the value of $\Theta = 90°$ indicates that the cylinder is at the vertical position. Table 5 shows that the reduced skin friction value and the reduced Nusselt number in consideration of all types of hybrid nanofluids decrease irregularly with increasing angles of Θ. However, it is noticeable that the magnitude of the reduced skin friction values is at the lowest and greatest values when $\Theta = 0°$ and $\Theta = 65°$, respectively, for all selected hybrid nanofluids. In addition, the table shows that Cu-GO/blood hybrid nanofluids ($C_f Re^{1/2} = 1.06396$) have the greatest magnitude of reduced skin friction, followed by Cu-GNP/blood ($C_f Re^{1/2} = 1.05484$) and Cu-graphene/blood ($C_f Re^{1/2} = 1.03985$) hybrid nanofluids at $\Theta = 65$. It is also notable to observe that the reduced Nusselt numbers are at the highest and lowest values when $\Theta = 0°$and $\Theta = 65°$, respectively, for all selected hybrid nanofluids. It can be clearly noticed that Cu-GNP/blood hybrid nanofluids ($Nu_x Re^{-1/2} = 23.02017$) have the greatest reduced skin friction, followed by Cu-GO/blood ($Nu_x Re^{-1/2} = 21.72835$) and Cu-graphene/blood ($Nu_x Re^{-1/2} = 21.72805$) hybrid nanofluids at $\Theta = 0°$.

Table 5: The repercussion of Θ on reduced skin friction value and reduced Nusselt number

Θ	$C_f\ Re^{1/2}$			$Nu_x Re^{-1/2}$		
	Graphene	GO	GNP	Graphene	GO	GNP
0	−0.65084	−0.60426	−0.62768	21.72805	21.72835	23.02017
20	−0.77713	−0.74958	−0.76435	21.63563	21.62144	22.91089
45	−0.75061	−0.71886	−0.73554	21.65499	21.64402	22.93390
65	−1.03985	−1.06396	−1.05484	21.44564	21.39290	22.68099
90	−1.00359	−1.01914	−1.01404	21.47160	21.42513	22.71298

The impact of value variations of ϕ_1 and ϕ_2 against the reduced skin friction value and the reduced Nusselt number are anticipated in Table 6. The values imposed on ϕ_1 and ϕ_2 are from 0.01 to 0.04. NF-A mono nanofluid represents the Cu/blood mono nanofluid with different values of ϕ_1 while NF-B, NF-C, and NF-D mono nanofluids represent the graphene/blood, GO/blood, and GNP/blood mono nanofluids with different values of ϕ_2, respectively. Moreover, HNF-AB, HNF-AC, and HNF-AD hybrid nanofluids represent the Cu-graphene/blood, Cu-GO/blood, and Cu-GNP/blood hybrid nanofluids when $\phi_1 = \phi_2$. In addition, HNF-AB1 until HNF-AB4, HNF-AC1 until HNF-AC4, and HNF-AD1 until HNF-AD4 are hybrid nanofluids that represent the Cu-graphene/blood, Cu-GO/blood, and Cu-GNP/blood hybrid nanofluids when $\phi_1 = 0.02$ and $0.01 \le \phi_2 \le 0.04$. Table 6 indicates that the reduced skin friction values incline for higher counts of ϕ_1 and ϕ_2 based on selected types of mono and hybrid nanofluids. These results further exhibit that the reduced Nusselt number increases with growing values of ϕ_2 for all mono and hybrid nanofluids except for NF-A (Cu/blood mono nanofluids). In addition, the result shows that NF-D (GNP/blood mono nanofluids) with $\phi_2 = 0.04$ has the highest magnitude of reduced skin friction and Nusselt number compared to other mono nanofluids types. Furthermore, the outcome exhibits that HNF-AD (Cu-GNP/blood hybrid nanofluids) has the highest Nusselt number compared to HNF-AB and HNF-AC when $\phi_1 = \phi_2$ are applied. Next, HNF-AD4 (Cu-GNP/blood hybrid nanofluids with $\phi_1 = 0.02$ and $\phi_2 = 0.04$) has the highest Nusselt number compared to other types of hybrid nanofluids. Thus, from the table data, it can be indicated that GNP nanoparticles with $n = 5.7$ enhance the heat transfer performance of Cu-GNP/blood hybrid nanofluid because of its' nanoplatelet shape that allows bigger nanoparticle surface area in contact with the cylindrical surface as compared to the spherical graphene and GO shapes.

Table 6: The repercussion of ϕ_1 and ϕ_2 on reduced skin friction and Nusselt number

Fluid	ϕ_1-Cu	ϕ_2-Graphene	ϕ_2-GO	ϕ_2-GNP	$C_f\ Re^{1/2}$	$Nu_x Re^{-1/2}$
F-A	0.01				−0.64840	19.88841
NF-A	0.02				−0.72954	19.81796
NF-A	0.03				−0.82111	19.74614
NF-A	0.04				−0.92522	19.67271
NF-B		0.01			−0.61075	20.51571
NF-B		0.02			−0.64815	21.08342
NF-B		0.03			−0.68850	21.66112
NF-B		0.04			−0.73209	22.24905
NF-C			0.01		−0.60825	20.51758
NF-C			0.02		−0.64282	21.08738
NF-C			0.03		−0.67996	21.66737
NF-C			0.04		−0.71993	22.25784
NF-D				0.01	−0.64522	20.95130
NF-D				0.02	−0.68553	21.98041
NF-D				0.03	−0.72913	23.01928
NF-D				0.04	−0.77638	24.06812
HNF-AB	0.01	0.01			−0.68797	20.44382
HNF-AB	0.02	0.02			−0.82373	20.93291
HNF-AB	0.03	0.03			−0.99073	21.42394
HNF-AB	0.04	0.04			−1.20004	21.91555
HNF-AC	0.01		0.01		−0.68524	20.44573
HNF-AC	0.02		0.02		−0.81728	20.93705
HNF-AC	0.03		0.03		−0.97907	21.43072
HNF-AC	0.04		0.04		−1.18082	21.92547
HNF-AD	0.01			0.01	−0.75714	20.82154
HNF-AD	0.02			0.02	−0.94893	21.69496
HNF-AD	0.03			0.03	−1.20556	22.54358
HNF-AD	0.04			0.04	−1.57310	23.35239
HNF-AB1	0.02	0.01			−0.77478	20.37067
HNF-AB2	0.02	0.02			−0.82373	20.93291
HNF-AB3	0.02	0.03			−0.87680	21.50481
HNF-AB4	0.02	0.04			−0.93444	22.08657
HNF-AC1	0.02		0.01		−0.77177	20.37260

(Continued)

Table 6 (continued)

Fluid	ϕ_1-Cu	ϕ_2-Graphene	ϕ_2-GO	ϕ_2-GNP	$C_f\ Re^{1/2}$	$Nu_x Re^{-1/2}$
HNF-AC2	0.02		0.02		−0.81728	20.93705
HNF-AC3	0.02		0.03		−0.86639	21.51139
HNF-AC4	0.02		0.04		−0.91950	22.09586
HNF-AD1	0.02			0.01	−0.88941	20.68531
HNF-AD2	0.02			0.02	−0.94893	21.69496
HNF-AD3	0.02			0.03	−1.01404	22.71298
HNF-AD4	0.02			0.04	−1.08547	23.73939

Table 7 displays the impacts of the parameters of γ, ζ, M, λ, Rd, H_w and Q on the reduced skin friction value and on the reduced Nusselt number when $\phi_1 = 0.02$ (for Cu) and $\phi_2 = 0.03$ (for graphene, GO, or GNP) are applied to the current model. Initially, the study assumes $\gamma = 1$, $\zeta = 0.4$, $M = 0.1$, $\lambda = 0.1$, $\Theta = 90$, $Rd = 4$, $H_w = 1$, and $Q = 0.1$ as the default values for these parameters. From Table 7, both reduced quantities decrease with higher values of γ, while an increase is observed with higher values of H_w. Conversely, the magnitudes of reduced skin friction and reduced Nusselt number increase and decrease with rising values of ζ and λ, respectively. However, the inverse is true for elevated values of M. Increases in Rd and Q appear not to influence the reduced skin friction values but they decrease the reduced Nusselt number in both instances. Notably, Cu-GNP/blood hybrid nanofluids exhibit the highest reduced skin friction coefficient compared to other chosen hybrid nanofluids for all parameters except the λ parameter. Furthermore, possessing the highest reduced Nusselt number for all parameters, Cu-GNP/blood hybrid nanofluids act as the superior heat flux conductor among other hybrid nanofluids used in this research.

Table 7: The repercussion of some imminent parameters on reduced skin friction and Nusselt number when $\phi_1 = 0.02$ and $\phi_2 = 0.03$ (for graphene, GO and GNP)

	Imminent parameters						$C_f Re^{1/2}$			$Nu_x Re^{-1/2}$		
γ	σ	M	λ	Rd	H_w	Q	Graphene	GO	GNP	Graphene	GO	GNP
1	0.4	0.1	0.1	4	1	0.1	−0.87680	−0.86639	−1.01404	21.50481	21.51139	22.71298
0							−1.84544	−1.81972	−2.01291	24.04101	24.04694	26.04351
1							−0.87680	−0.86639	−1.01404	21.50481	21.51139	22.71298
2							−0.64615	−0.63904	−0.72600	19.47543	19.48278	20.54381
3							−0.53452	−0.52895	−0.59363	17.94286	17.95041	18.91598
	0.2						−0.80542	−0.79714	−0.90662	21.52965	21.53570	22.75439
	0.4						−0.87680	−0.86639	−1.01404	21.50481	21.51139	22.71298
	0.6						−0.97313	−0.95929	−1.17821	21.47467	21.48199	22.65896
	0.8						−1.11654	−1.09604	−1.49871	21.43650	21.44493	22.58134

(Continued)

Table 7 (continued)

Imminent parameters							$C_f Re^{1/2}$			$Nu_x Re^{-1/2}$		
γ	σ	M	λ	Rd	H_w	Q	Graphene	GO	GNP	Graphene	GO	GNP
		0.1					−0.87680	−0.86639	−1.01404	21.50481	21.51139	22.71298
		0.2					−0.81884	−0.80871	−0.95216	21.54089	21.54751	22.75325
		0.3					−0.76145	−0.75156	−0.89116	21.57751	21.58415	22.79415
		0.4					−0.70449	−0.69479	−0.83085	21.61467	21.62136	22.83572
			0				−0.87680	−0.86639	−0.87332	21.56309	21.53592	22.82413
			0.1				−1.00359	−1.01914	−1.01404	21.47160	21.42513	22.71298
			0.2				−1.15810	−1.21492	−1.19014	21.36164	21.28544	22.57575
			0.3				−1.36087	−1.50019	−1.43367	21.22034	21.08741	22.39008
				4			−0.87680	−0.86639	−1.01404	21.50481	21.51139	22.71298
				5			−0.87680	−0.86639	−1.01404	21.41267	21.42131	22.56605
				6			−0.87680	−0.86639	−1.01404	21.30482	21.31565	22.39627
				7			−0.87680	−0.86639	−1.01404	21.18653	21.19959	22.21194
					−1		−0.45919	−0.45643	−0.51375	0.27811	0.28131	0.20233
					−0.5		−0.53064	−0.52689	−0.59602	2.32975	2.33566	2.33611
					0.5		−0.73163	−0.72440	−0.83414	13.29991	13.30723	13.98693
					1		−0.87680	−0.86639	−1.01404	21.50481	21.51139	22.71298
						0.1	−0.87680	−0.86639	−1.01404	21.50481	21.51139	22.71298
						0.2	−0.87680	−0.86639	−1.01404	20.93821	20.94550	22.07696
						0.3	−0.87680	−0.86639	−1.01404	20.33610	20.34431	21.39490
						0.4	−0.87680	−0.86639	−1.01404	19.69045	19.69989	20.65346

5 Conclusion

This study examines the effects of thermal radiation and heating sources on non-Newtonian Sutterby hybrid nanofluids consisting of various types of graphene, GO, and GNP with Cu-blood over a slanted permeable cylinder. Initially, the governing PDEs of the fluid model are transformed into nonlinear ordinary DEs using analogous transformational terms. Subsequently, they are addressed with the bvp4c scheme in MATLAB to obtain numerical solutions. The effects of other pertinent parameters on the Sutterby non-Newtonian blood nanofluids are also assessed and presented in figures and tables. The results are as follows:

- The velocity distributions increase with increasing values of γ and M, but decrease for higher values of ϕ_2, ζ, λ and H_w.
- The temperature distributions rise for greater values of ϕ_2, γ, ζ, λ, Rd and Q, but diminish for higher M and H_w.
- Cu-graphene/blood hybrid nanofluids exhibit the highest velocity but the lowest temperature distribution, while Cu-GNP/blood hybrid nanofluids show the lowest velocity and the highest temperature distributions for all values of ϕ_2.

- Cu-GO/blood hybrid nanofluids have the greatest velocity distributions, followed by Cu-graphene/blood hybrid nanofluids, while Cu-GNP/blood hybrid nanofluids display the lowest velocity distribution for all values of γ, ζ, M and H_w parameters except for the λ parameter.
- Cu-GNP/blood hybrid nanofluids possess the maximum temperature distribution, followed by Cu-graphene/blood and Cu-GO/blood hybrid nanofluids for γ, ζ, M, Rd, H_w, and Q parameters, except in the case of the λ parameter.
- The magnitude of the reduced skin friction values is at its minimum and maximum when $\Theta = 0°$ and $\Theta = 65°$, while the opposing results of the reduced Nusselt number are observed at $\Theta = 0°$ and $\Theta = 65°$ for all hybrid nanofluids used in this study.
- Both magnitude quantities of reduced skin friction and reduced Nusselt number increase for greater values of ϕ_2. However, the reduced Nusselt number decreases for a greater copper nanoparticle volume fraction, ϕ_1.
- HNF-AD4 (Cu-GNP/blood hybrid nanofluid with $\phi_1 = 0.02$ and $\phi_2 = 0.04$) boasts the highest Nusselt number compared to other types of hybrid nanofluids.
- Thus, GNPs (with the nanoplatelet shape factor $n = 5.7$) are highly recommended to enhance the heat transfer performance of blood-based hybrid nanofluids as they contribute approximately 5% on average and up to 7.8% higher reduced Nusselt number compared to other nanoparticles of graphene and GO.
- The reduced skin friction value rises with higher values of ζ, λ and H_w, but decreases for higher values of γ and M.
- The reduced Nusselt number increases for increasing values of M and H_w, but decreases for higher values of γ, ζ, λ, Rd and Q.

Several potential applications arise from these research findings. For example, guidance for evaluating occupational and public health risks related to radiation and electromagnetic field exposure can be based on blood studies in rats. Moreover, the nanoparticles selected for this study can be particularly effective in medical treatments such as cancer therapy, anti-infection measures, and drug delivery. Hence, they promise to enhance medical systems, equipment, and devices. Nevertheless, further research in this domain must address the study's limitations and comprehensively meet industrial objectives and practical requirements.

Acknowledgement: Authors highly appreciate the contributions made by reviewers towards the final improvement of this manuscript.

Funding Statement: This research is funded by the Ministry of Higher Education, Malaysia, through the Research Fund of Fundamental Research Grant Scheme (FRGS/1/2020/STG06/UM/02/1: FP009-2020).

Author Contributions: Conceptualization, N.F.M.N.; methodology, S.N.A.G.; validation, S.N.A.G.; formal analysis, S.N.A.G.; investigation, S.N.A.G. and N.F.M.N.; data curation, S.N.A.G.; writing—original draft preparation, S.N.A.G.; writing—review and editing, N.F.M.N.; visualization, S.N.A.G.; supervision, N.F.M.N.; project administration, N.F.M.N.; funding acquisition, N.F.M.N. All authors have read and consented the finalized version of the manuscript.

Availability of Data and Materials: The present study utilizes data simulation with the numerical results as presently calculated.

Conflicts of Interest: The authors declare that they have no conflicts of interest to report regarding the present study.

References

1. Yamaguchi, H. (2008). *Engineering fluid mechanics*, vol. 85. Dordrecht, Netherlands: Springer Science & Business Media.
2. Choi, S. U., Eastman, J. A. (1995). *Enhancing Thermal Conductivity of Fluids with Nanoparticles*. Argonne National Lab (ANL), Argonne, IL, USA.
3. Sarkar, J., Ghosh, P., Adil, A. (2015). A review on hybrid nanofluids: Recent research, development and applications. *Renewable and Sustainable Energy Reviews, 43,* 164–177.
4. Babu, J. R., Kumar, K. K., Rao, S. S. (2017). State-of-art review on hybrid nanofluids. *Renewable and Sustainable Energy Reviews, 77,* 551–565.
5. Manjunatha, S., Kuttan, B. A., Jayanthi, S., Chamkha, A., Gireesha, B. J. (2019). Heat transfer enhancement in the boundary layer flow of hybrid nanofluids due to variable viscosity and natural convection. *Heliyon, 5(4),* e01469.
6. Nadeem, S., Abbas, N., Malik, M. Y. (2020). Inspection of hybrid based nanofluid flow over a curved surface. *Computer Methods and Programs in Biomedicine, 189,* 105193.
7. Salah, Y., Al Mukbel, O., Sabsabi, Y., Saranya, S., Al-Mdallal, Q. M. et al. (2023). Influence of PST and PHF heating conditions on the swirl flow of Al+Mg+TiO_2 ternary hybrid water-ethylene glycol based nanofluid with a rotating cone. *International Journal of Thermofluids, 19,* 100371.
8. Akhtar, S., Hussain, Z., Nadeem, S., Najjar, I. R., Sadoun, A. M. (2023). CFD analysis on blood flow inside a symmetric stenosed artery: Physiology of a coronary artery disease. *Science Progress, 106(2)*.
9. McCash, L. B., Akhtar, S., Nadeem, S., Saleem, S. (2021). Entropy analysis of the peristaltic flow of hybrid nanofluid inside an elliptic duct with sinusoidally advancing boundaries. *Entropy, 23(6),* 732.
10. Tripathi, J., Vasu, B., Bég, O. A. (2021). Computational simulations of hybrid mediated nano-hemodynamics (Ag-Au/Blood) through an irregular symmetric stenosis. *Computers in Biology and Medicine, 130,* 104213.
11. Sharma, B. K., Kumawat, C., Vafai, K. (2022). Computational biomedical simulations of hybrid nanoparticles (Au-Al_2O_3/blood-mediated) transport in a stenosed and aneurysmal curved artery with heat and mass transfer: Hematocrit dependent viscosity approach. *Chemical Physics Letters, 800,* 139666.
12. Akram, J., Akbar, N. S., Tripathi, D. (2020). Blood-based graphene oxide nanofluid flow through capillary in the presence of electromagnetic fields: A sutterby fluid model. *Microvascular Research, 132,* 104062.
13. Waqas, H., Farooq, U., Alghamdi, M., Muhammad, T. (2022). Significance of melting process in magnetized transport of hybrid nanofluids: A three-dimensional model. *Alexandria Engineering Journal, 61(5),* 3949–3957.
14. Al-Mughanam, T., Almaneea, A. (2022). Numerical study on thermal efficiencies in mono, hybrid and tri-nano sutterby fluids. *International Communications in Heat and Mass Transfer, 138,* 106348.
15. Bouslimi, J., Alkathiri, A. A., Alharbi, A. N., Jamshed, W., Eid, M. R. et al. (2022). Dynamics of convective slippery constraints on hybrid radiative sutterby nanofluid flow by galerkin finite element simulation. *Nanotechnology Reviews, 11(1),* 1219–1236.
16. Jamshed, W., Safdar, R., Rehman, Z., Lashin, M. M., Ehab, M. et al. (2022). Computational technique of thermal comparative examination of Cu and Au nanoparticles suspended in sodium alginate as Sutterby nanofluid via extending PTSC surface. *Journal of Applied Biomaterials & Functional Materials, 20*.
17. Tiwari, R. K., Das, M. K. (2007). Heat transfer augmentation in a two-sided lid-driven differentially heated square cavity utilizing nanofluids. *International Journal of Heat and Mass Transfer, 50(9–10),* 2002–2018.
18. Dinarvand, S., Rostami, M. N. (2019). Mixed convection of a Cu-Ag/water hybrid nanofluid along a vertical porous cylinder via modified Tiwari-Das model. *Journal of Theoretical and Applied Mechanics, 49(2),* 149–169.

19. Dinarvand, S., Rostami, M. N., Pop, I. (2019). A novel hybridity model for TiO_2-CuO/water hybrid nanofluid flow over a static/moving wedge or corner. *Scientific Reports, 9(1),* 16290.
20. Ramzan, M., Shahmir, N., Ghazwani, H. A. S. (2022). Hybrid nanofluid flow comprising spherical shaped particles with hall current and irreversibility analysis: An application of solar radiation. *Waves in Random and Complex Media*. https://doi.org/10.1080/17455030.2022.2123571
21. Alwawi, F. A., Al Faqih, F. M., Swalmeh, M. Z., Ibrahim, M. A. H. (2022). Combined convective energy transmission performance of Williamson hybrid nanofluid over a cylindrical shape with magnetic and radiation impressions. *Mathematics, 10(17),* 3191.
22. Saranya, S., Duraihem, F. Z., Isaac Lare, A. L., Al-Mdallal, Q. M. (2023). Quartic autocatalysis on horizontal surfaces with an asymmetric concentration: Water-based ternary-hybrid nanofluid carrying titania, copper, and alumina nanoparticles. *Physica Scripta, 98(7),* 075214.
23. Arshad, A., Jabbal, M., Yan, Y., Reay, D. (2019). A review on graphene based nanofluids: Preparation, characterization and applications. *Journal of Molecular Liquids, 279,* 444–484.
24. Smaisim, G. F., Abed, A. M., Al-Madhhachi, H., Hadrawi, S. K., Al-Khateeb, H. M. M. et al. (2023). Graphene-based important carbon structures and nanomaterials for energy storage applications as chemical capacitors and supercapacitor electrodes: A review. *BioNanoScience, 13(1),* 219–248.
25. Shafiee, A., Iravani, S., Varma, R. S. (2022). Graphene and graphene oxide with anticancer applications: Challenges and future perspectives. *MedComm, 3(1),* e118.
26. Mehrali, M., Sadeghinezhad, E., Akhiani, A. R., Latibari, S. T., Metselaar, H. S. C. et al. (2017). Heat transfer and entropy generation analysis of hybrid graphene/Fe_3O_4 ferro-nanofluid flow under the influence of a magnetic field. *Powder Technology, 308,* 149–157.
27. Sadeghinezhad, E., Mehrali, M., Saidur, R., Mehrali, M., Latibari, S. T. et al. (2016). A comprehensive review on graphene nanofluids: Recent research, development and applications. *Energy Conversion and Management, 111,* 466–487.
28. Purbia, D., Khandelwal, A., Kumar, A., Sharma, A. K. (2019). Graphene-water nanofluid in heat exchanger: Mathematical modelling, simulation and economic evaluation. *International Communications in Heat and Mass Transfer, 108,* 104327.
29. Ghani, S. N. A., Yarmand, H., Noor, N. F. M. (2023). Assorted graphene-based nanofluid flows near a reversed stagnation point over an inclined permeable cylinder. *Proceedings of the National Academy of Sciences, India Section A: Physical Sciences, 93(1),* 43–55.
30. Xiao, W., Zhai, X., Ma, P., Fan, T., Li, X. (2018). Numerical study on the thermal behavior of graphene nanoplatelets/epoxy composites. *Results in Physics, 9,* 673–679.
31. Massoudi, M. D., Ben Hamida, M. B., Almeshaal, M. A. (2021). Free convection and thermal radiation of nanofluid inside nonagon inclined cavity containing a porous medium influenced by magnetic field with variable direction in the presence of uniform heat generation/absorption. *International Journal of Numerical Methods for Heat & Fluid Flow, 31(3),* 933–958.
32. Kierzenka, J., Shampine, L. F. (2001). A BVP solver based on residual control and the maltab PSE. *ACM Transactions on Mathematical Software, 27(3),* 299–316.
33. Shampine, L. F., Kierzenka, J., Reichelt, M. W. (2000). Solving boundary value problems for ordinary differential equations in MATLAB with bvp4c. *Tutorial Notes, 2000,* 1–27.